Electronic Supplementary Information (ESI)

MOF-Derived Zn-Mn Mixed Oxides@Carbon Hollow Disks with Robust Hierarchical Structure for High-Performance Lithium-Ion Batteries

Dong Wang,[a,b] Weiwei Zhou,*[,b] Rui Zhang,[a] Xiaoxiao Huang,[a] Jinjue Zeng,[b] Yanfang Mao,[c] Chunyan Ding,[a] Jian Zhang,[b] Jinping Liu,[c] and Guangwu Wen*[,a,d,e]

[a]School of Materials Science and Engineering, Harbin Institute of Technology, Harbin 150001, China.

[b]School of Materials Science and Engineering, Harbin Institute of Technology at Weihai, Weihai 264209, China.

[c]School of Chemistry, Chemical Engineering and Life Science and State Key Laboratory of Advanced Technology for Materials Synthesis and Processing, Wuhan University of Technology, Wuhan, Hubei 430070, China.

[d]School of Materials Science and Engineering, Shandong University of Technology, Zibo 255000, China.

[e]Shandong Industrial Ceramics Research & Design Institute Co., Ltd. No.128 Yumin Road, Zibo 255000, China.

*E-mail: g_wen2016@163.com; zhouweiwei@hit.edu.cn

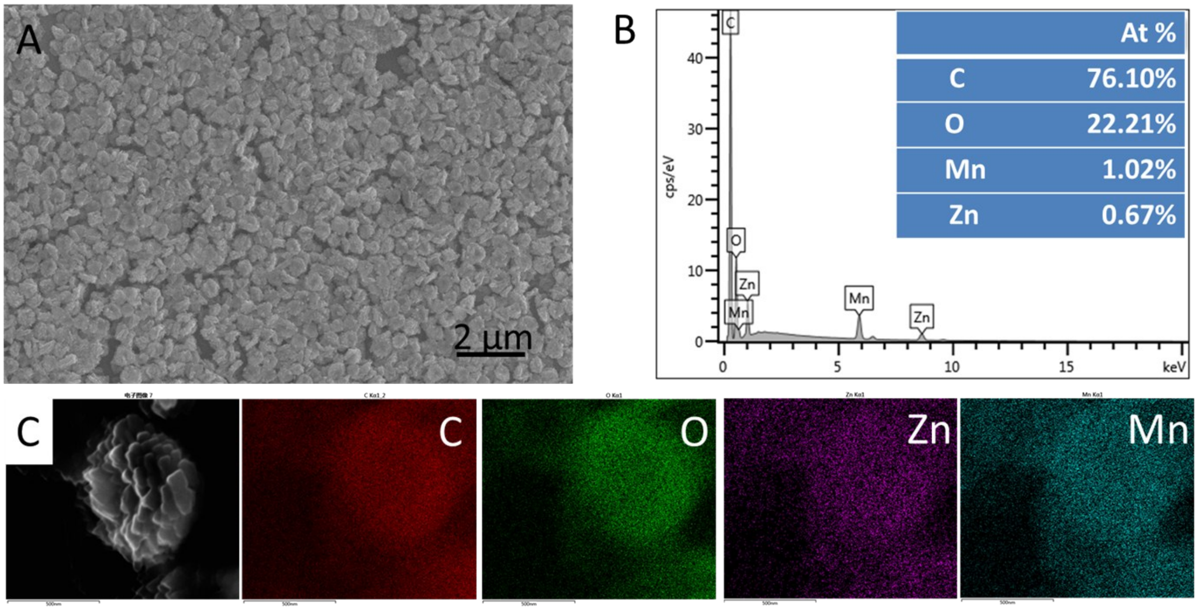

Fig. S1 (A) Low-magnification FESEM image of the as-prepared Zn-Mn-BTC-0.5 precursor, indicating the uniform size and disk-like morphology. (B) EDX spectrum of the Zn-Mn-BTC-0.5 precursor. (C) STEM image of Zn-Mn-BTC-0.5 precursor and corresponding element mapping images of C, O, Zn, and Mn.

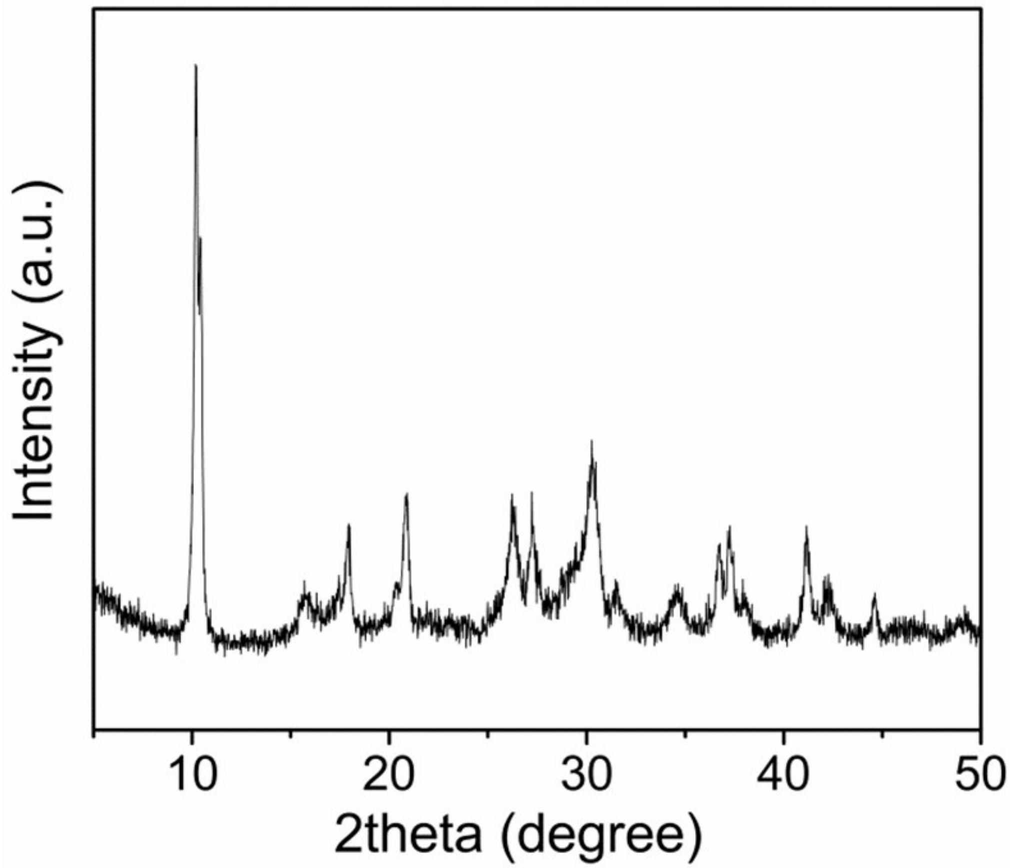

Fig. S2 XRD pattern of the as-prepared Zn-Mn-BTC-0.5.

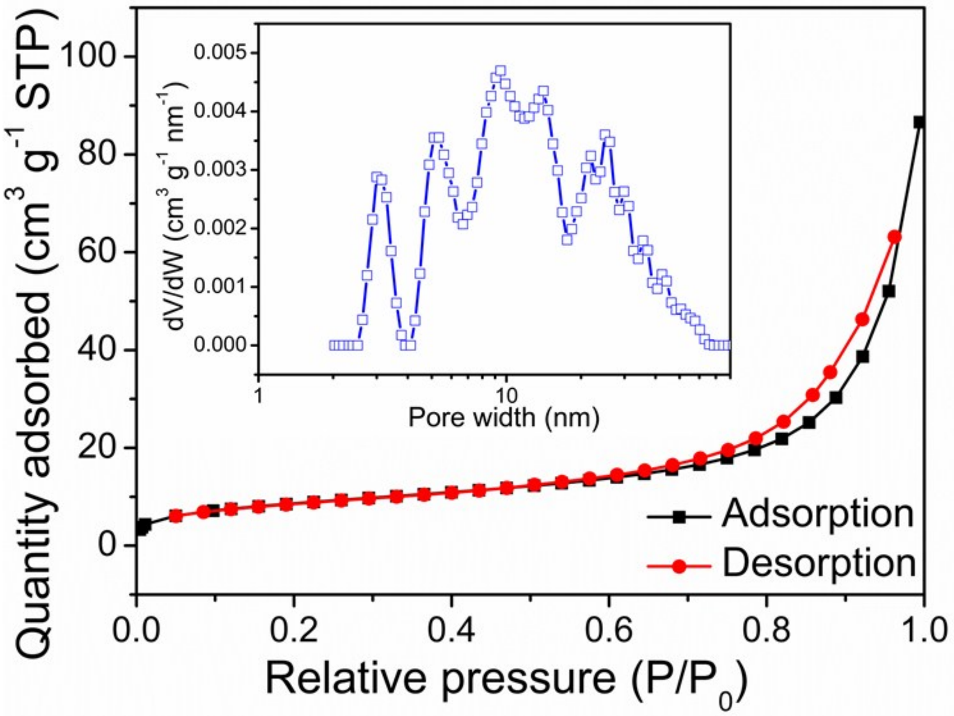

Fig. S3 N_2 adsorption-desorption isotherms of Zn-Mn-BTC-0.5. The inset shows the pore size distribution plot calculated using the NLDFT model.

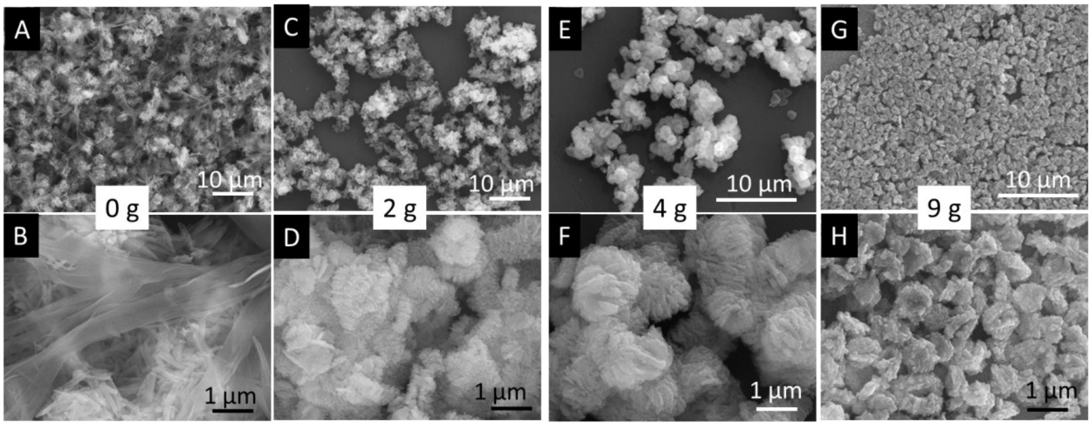

Fig. S4 FESEM images of the co-precipitation products with different amounts of PVP: (A, B) 0 g, (C, D) 2 g, (E, F) 4 g, (G, H) 9 g, indicating the important role of PVP in forming discrete hollow nanodisks.

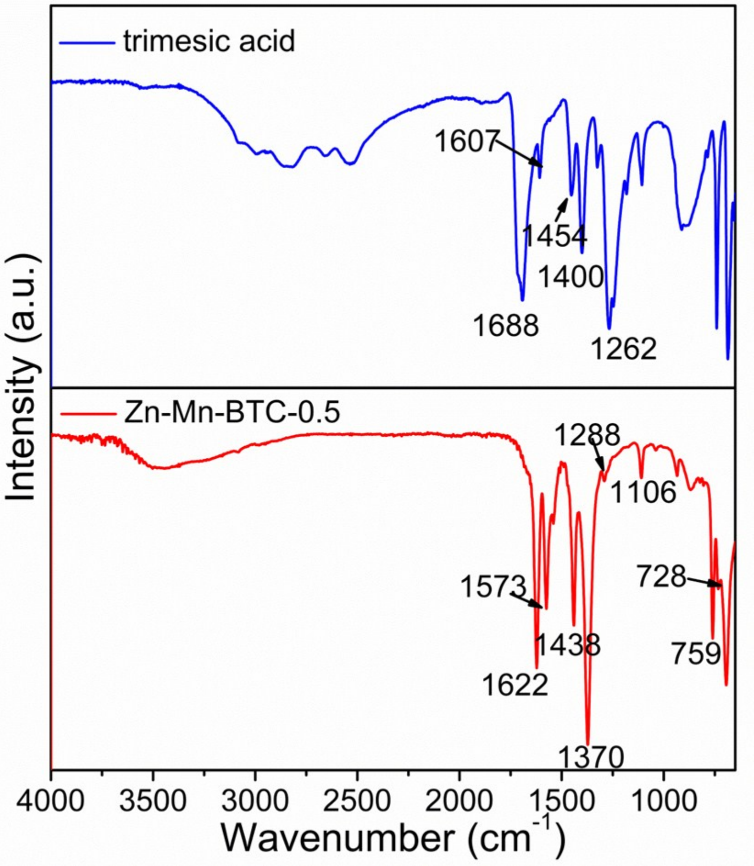

Fig. S5 FTIR spectra of trimesic acid and Zn-Mn-BTC-0.5. In the FTIR spectrum of trimesic acid, the weak bands between 3100-2500 cm^{-1} shoulde be assigned to O-H stretching of carboxy groups, and the bands of carboxy groups at 1688 and 1262 cm^{-1} are assigned to C=O stretching and C-O stretching, respectively. The three bands at 1607, 1454, and 1400 cm^{-1} are attributed to characteristic vibrations of benzene groups.

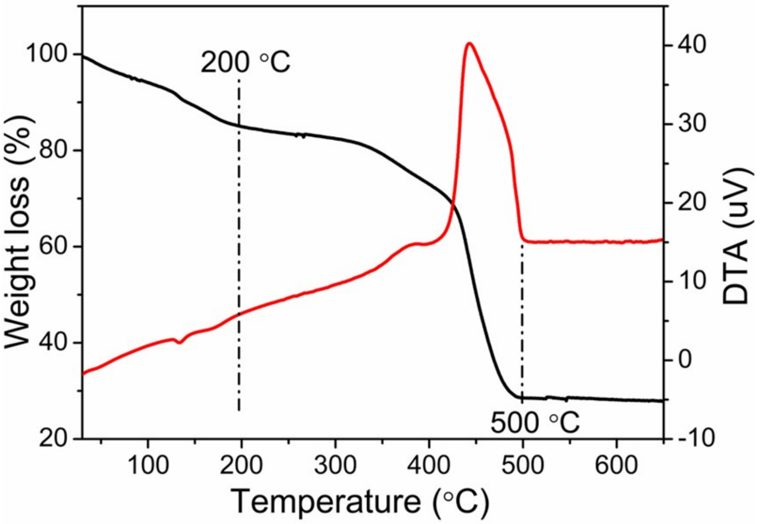

Fig. S6 DTA-TG curves of Zn-Mn-BTC-0.5 HHNDs measured in Ar flow. The weight loss below 200 ℃ should be attributed to the removal of physisorbed moisture or solvent molecules. The weight loss in the range of 200-500 ℃ corresponds to the decomposition and carbonization of Zn-Mn-BTC MOFs.

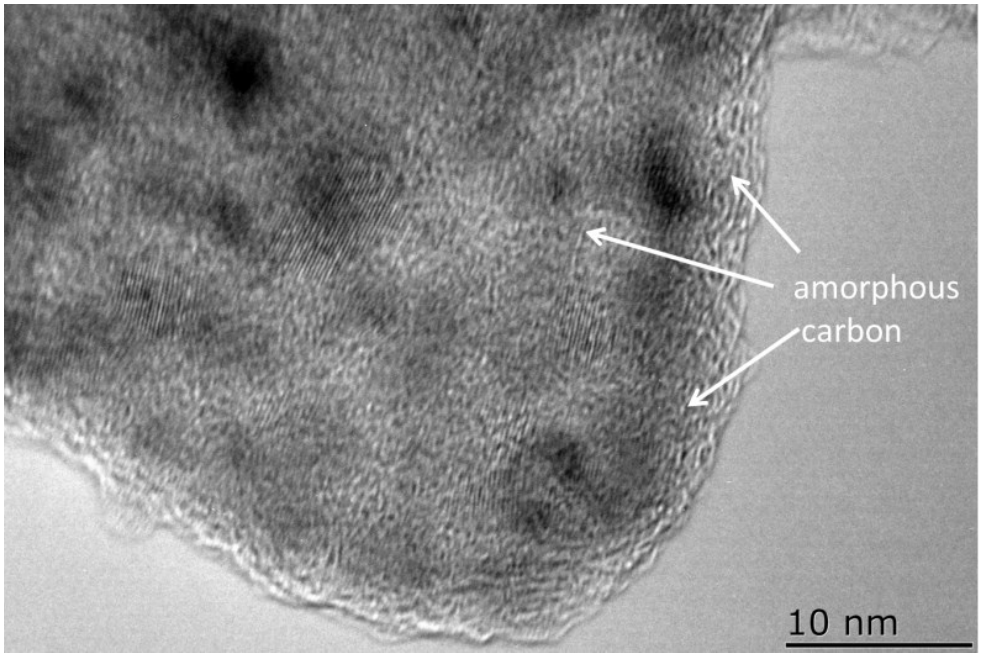

Fig. S7 HRTEM image of the $Zn_{0.5}MnO@C$ HHNDs.

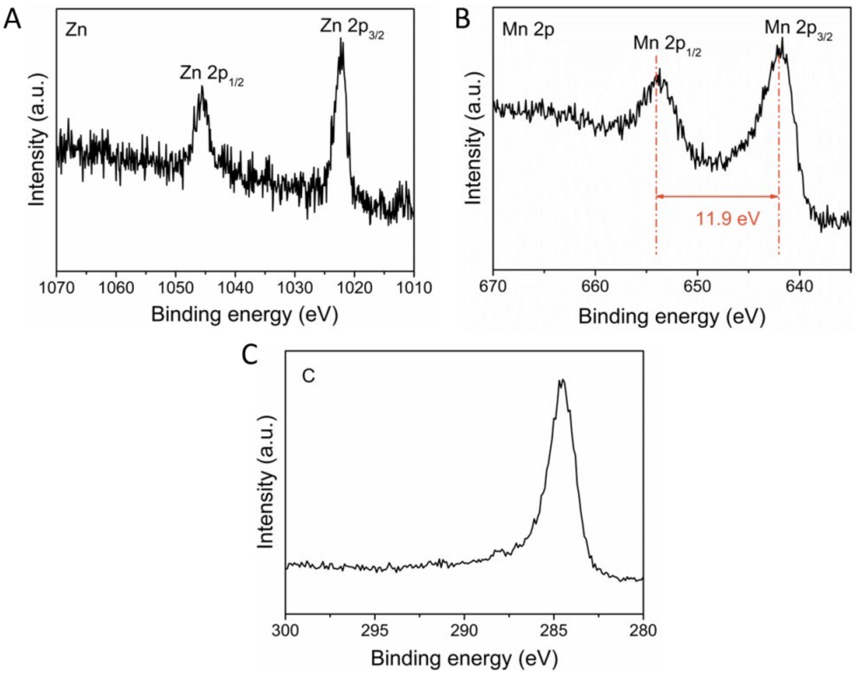

Fig. S8 High-resolution XPS spectra of (A) Zn 2p, (B) Mn 2p, and (C) C 1s of hierarchical $Zn_{0.5}MnO$@C HHNDs.

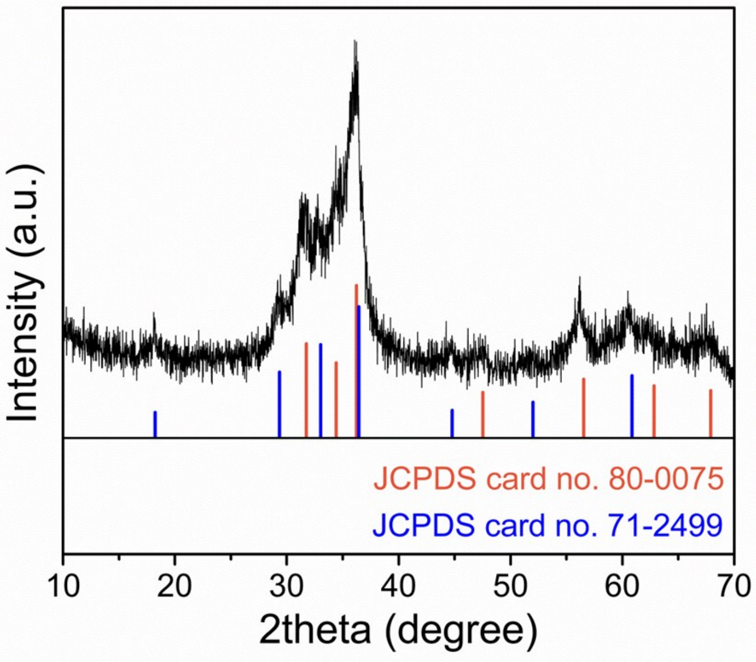

Fig. S9 XRD pattern of $Zn_{0.5}MnO$@C HHNDs.

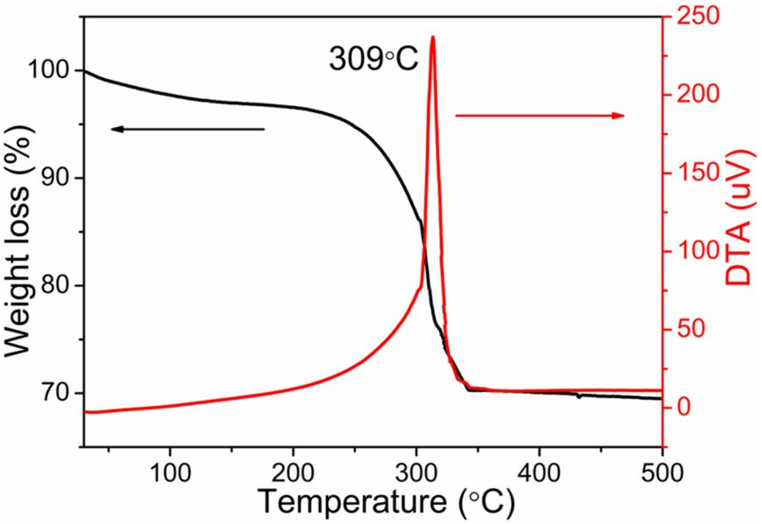

Fig. S10 DTA-TG curves of hierarchical $Zn_{0.5}MnO$@C HHNDs measured in air.

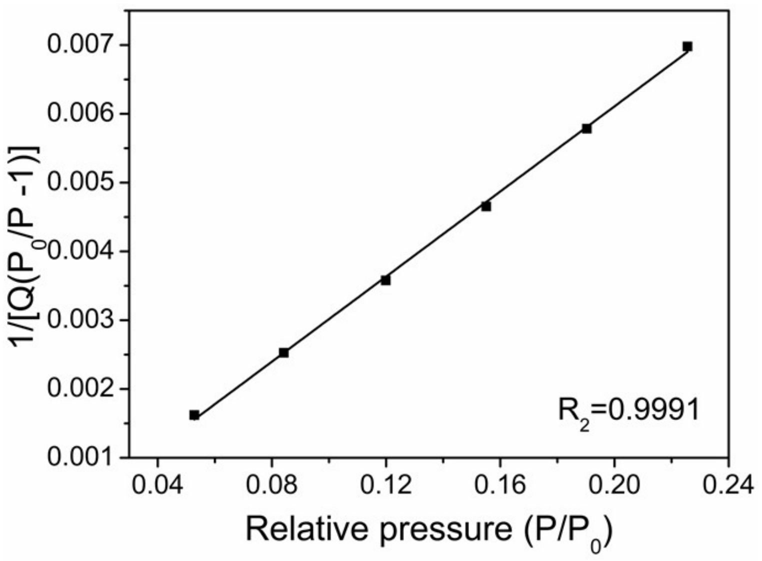

Fig. S11 BET plot of $Zn_{0.5}MnO@C$ HHNDs.

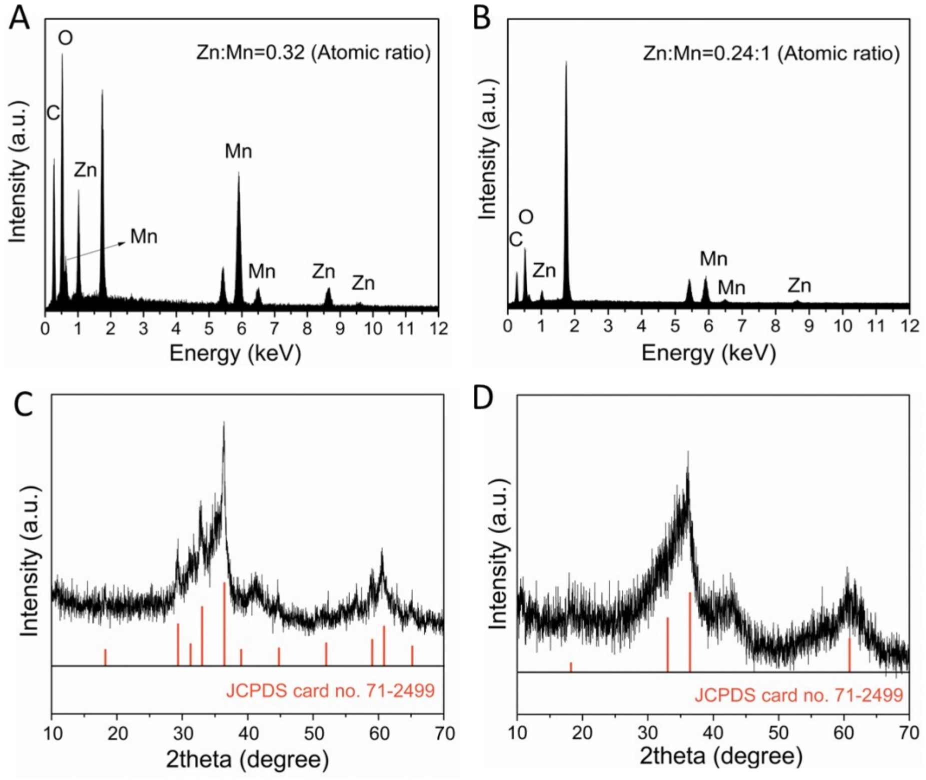

Fig. S12 EDX spectra of (A) $Zn_{0.32}MnO@C$ and (B) $Zn_{0.24}MnO@C$. XRD patterns of (C) $Zn_{0.32}MnO@C$ and (D) $Zn_{0.24}MnO@C$. The absence of ZnO phase in the XRD patterns of $Zn_{0.32}MnO@C$ and $Zn_{0.24}MnO@C$ indicates that the zinc atoms are completely incorporated into the Mn_3O_4 lattice.

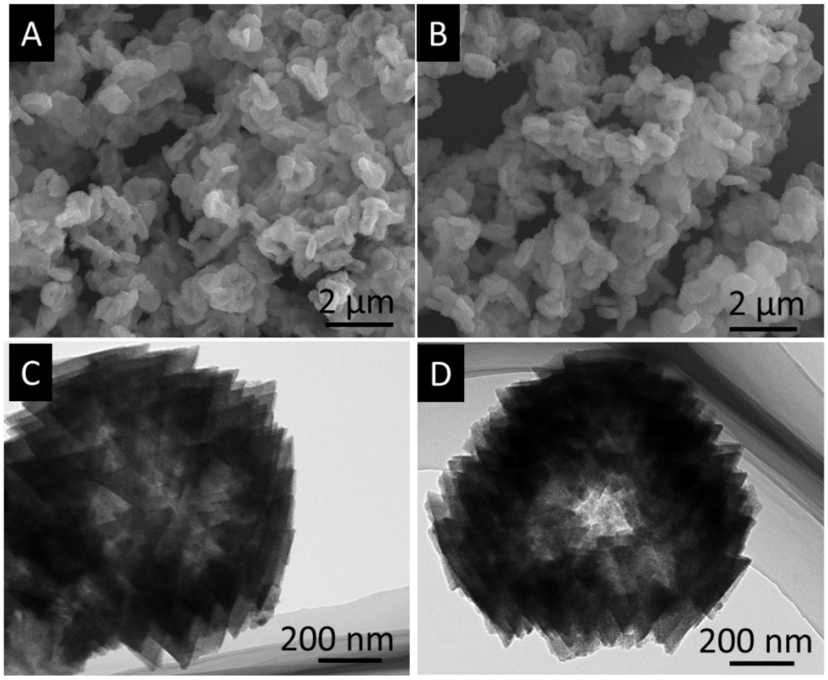

Fig. S13 FESEM images of (A) $Zn_{0.32}MnO@C$ and (B) $Zn_{0.24}MnO@C$. TEM images of (C) $Zn_{0.32}MnO@C$ and (D) $Zn_{0.24}MnO@C$.

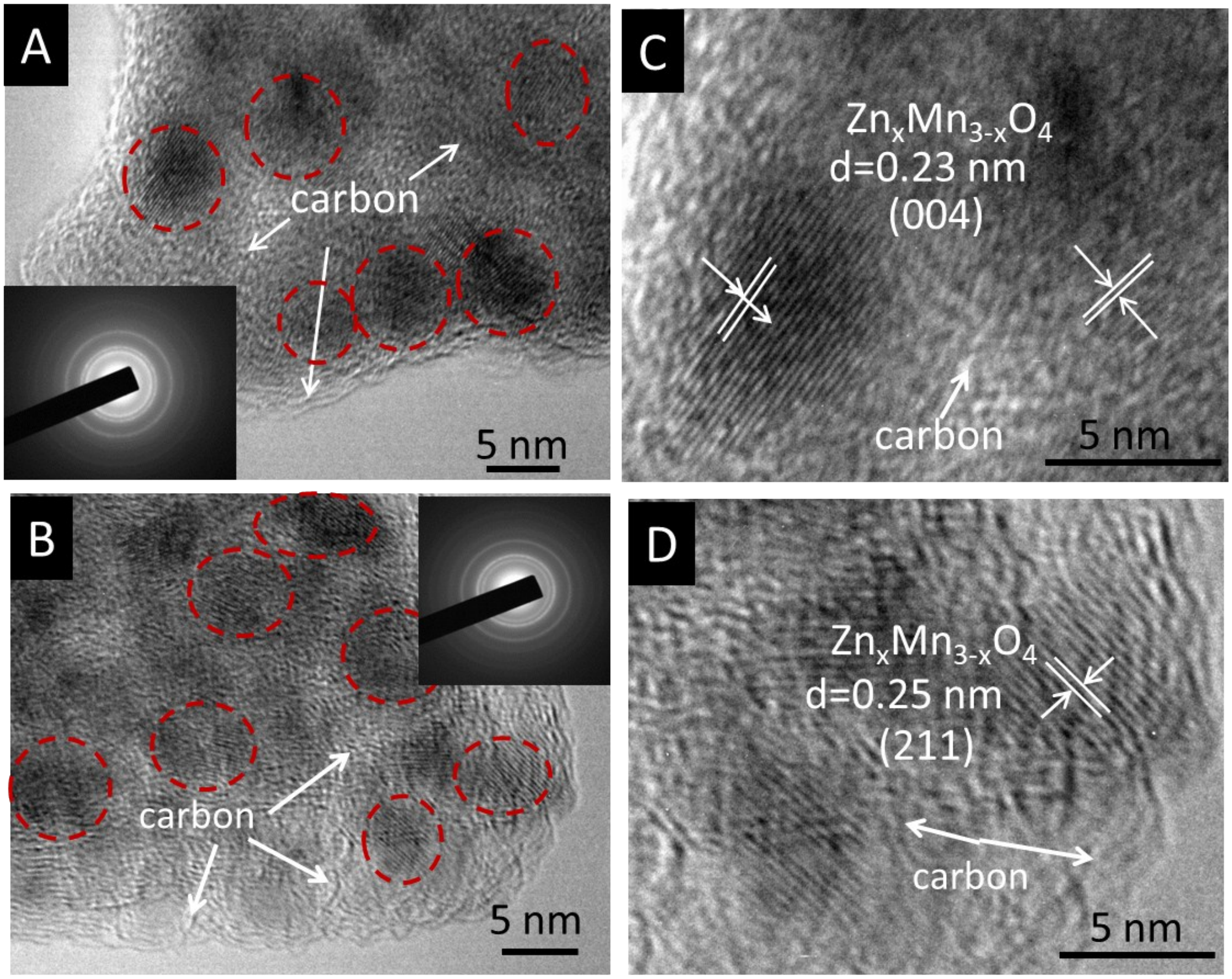

Fig. S14 HRTEM images of (A, C) $Zn_{0.32}MnO@C$ and (B, D) $Zn_{0.24}MnO@C$. The insets of A and B show the corresponding SAED patterns. For these two samples, the HRTEM images reveal that ultrafine $Zn_xMn_{3-x}O_4$ nanoparticles are homogeneously embedded in amorphous carbon matrix, while the distinct lattice fringes with interplanar distances of 0.23 and 0.25 nm can be assigned to the (004) and (211) planes of $Zn_xMn_{3-x}O_4$, respectively.

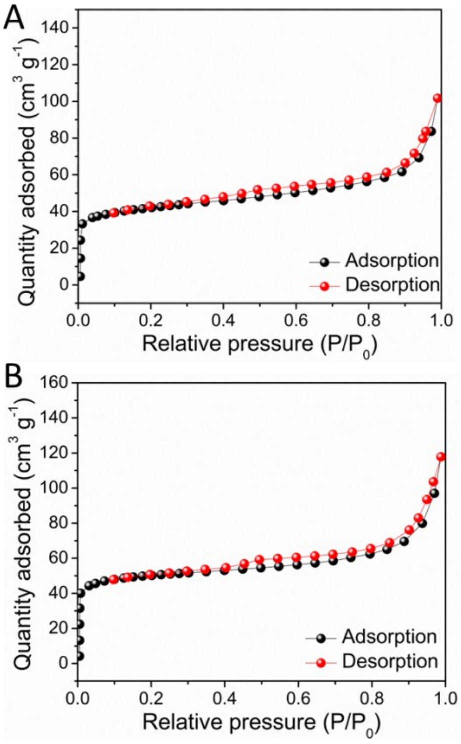

Fig. S15 Nitrogen adsorption-desorption isotherms of (A) $Zn_{0.32}MnO@C$ and (B) $Zn_{0.24}MnO@C$.

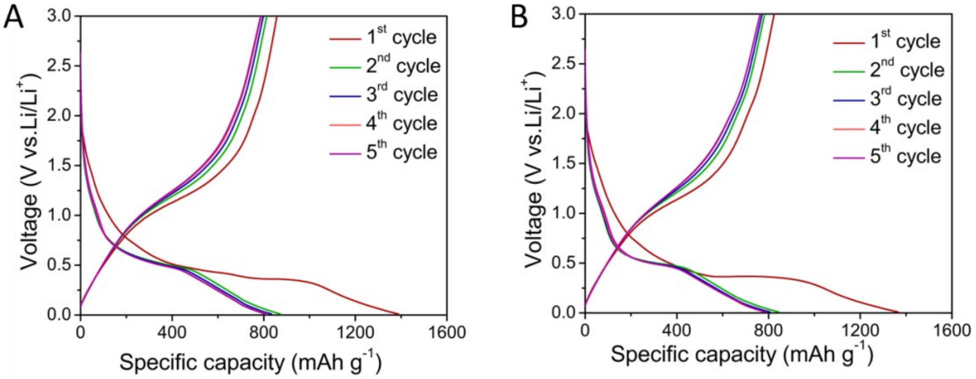

Fig. S16 Galvanostatic discharge-charge curves of (A) $Zn_{0.32}MnO$@C and (B) $Zn_{0.24}MnO$@C electrodes at a current density of 0.1 A g^{-1} for the initial 5 cycles.

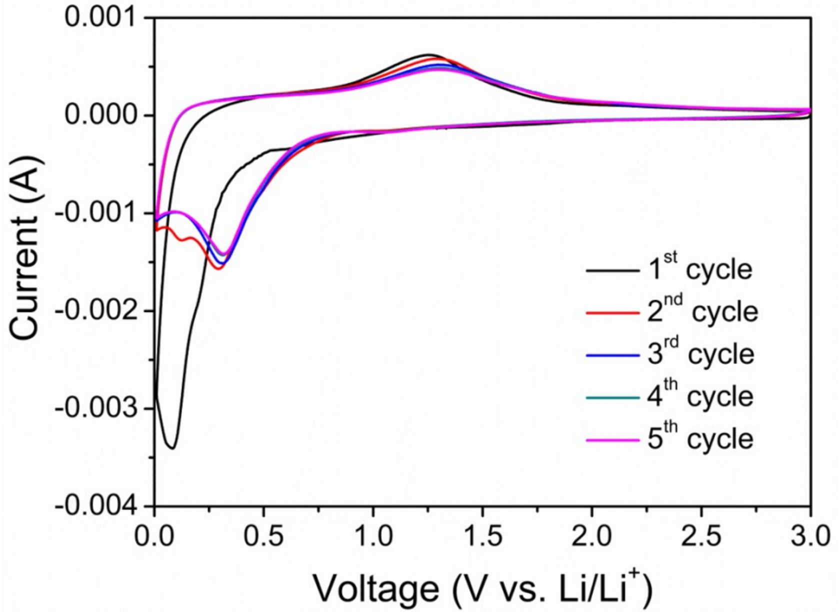

Fig. S17 Cyclic voltammetry curves of $Zn_{0.5}MnO$@C electrode at a scan rate of 0.1 mV s^{-1} in the potential range of 0.01-3.0 V.

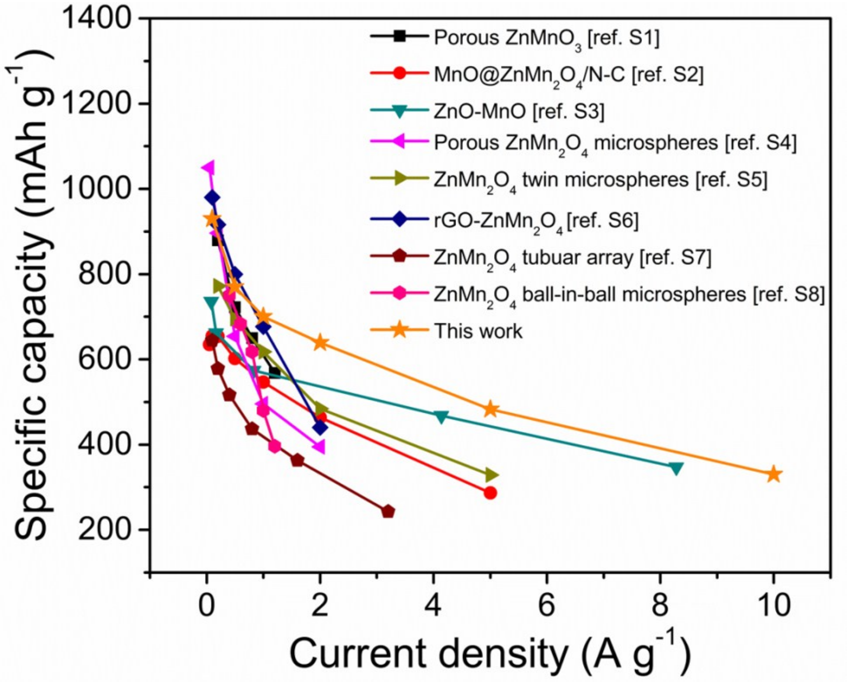

Fig. S18 Comparison of rate capabilities of hierarchical $Zn_{0.5}MnO@C$ electrode in this work and previously reported Zn-Mn mixed oxides-based electrodes.

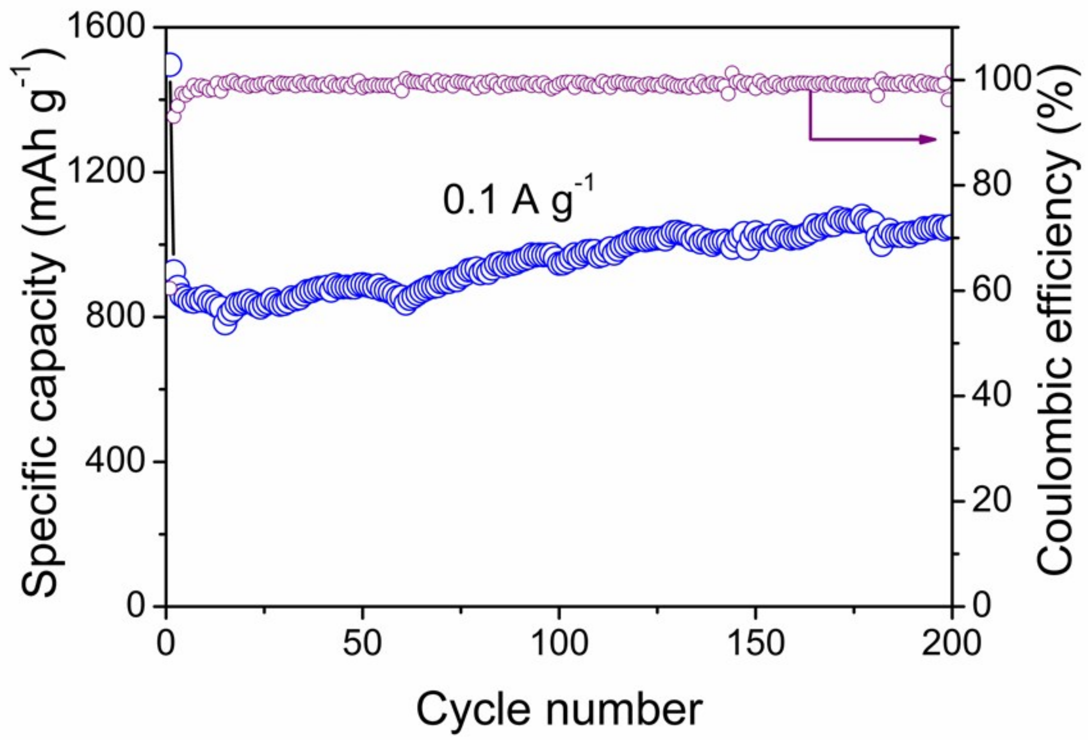

Fig. S19 Cycling performance of $Zn_{0.5}MnO@C$ electrode with corresponding Coulombic efficiency at a low current density of 0.1 A g^{-1}.

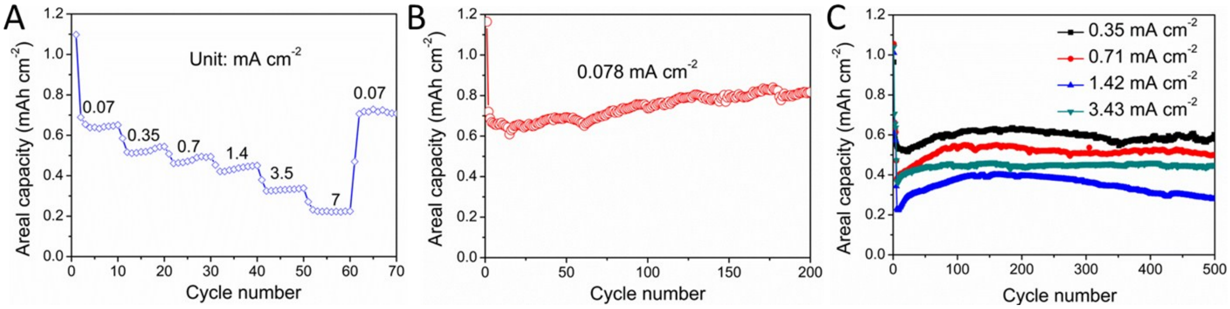

Fig. S20 Electrochemical performance of hierarchical $Zn_{0.5}MnO@C$ composites: (A) Rate capabilities at current densities from 0.07 to 7 mA cm^{-2}; (B) Cycling performance at a current density of 0.078 mA cm^{-2}; (C) Cycling performance at current densities of 0.35, 0.71, 1.42, and 3.43 mA cm^{-2}, respectively.

The average areal capacities of $Zn_{0.5}MnO@C$ HHNDs are 0.66, 0.54, 0.49, 0.45, 0.34, and 0.23 mAh cm^{-2} at current densities of 0.07, 0.35, 0.7, 1.4, 3.5, and 7 mA cm^{-2}, respectively. The reversible areal capacity at a current density of 0.078 mA cm^{-2} after 200 cycles is 0.82 mAh cm^{-2}. Moreover, the $Zn_{0.5}MnO@C$ HHNDs could deliver 0.60, 0.50, 0.45, and 0.28 mAh cm^{-2} after 500 cycles at current densities of 0.35, 0.71, 1.42, and 3.43 mA cm^{-2}, respectively.

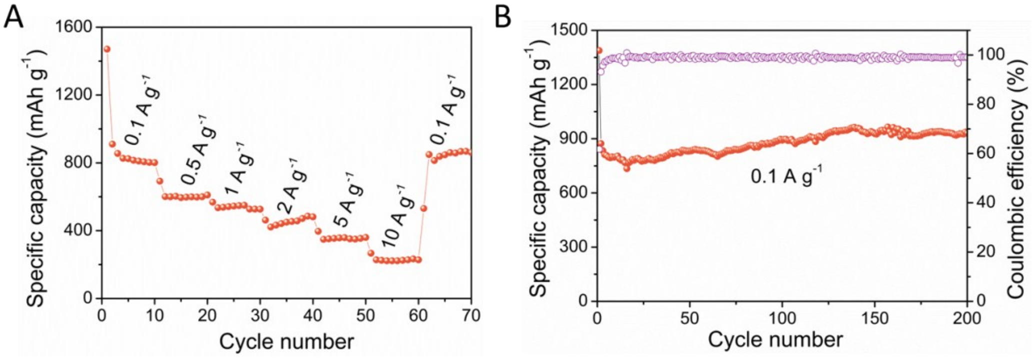

Fig. S21 Electrochemical performance of $Zn_{0.32}MnO$@C HHNDs as anode materials of LIBs: (A) rate capability at various current densities and (B) cycling performance with corresponding Coulombic efficiency at a current density of 0.1 A g^{-1}.

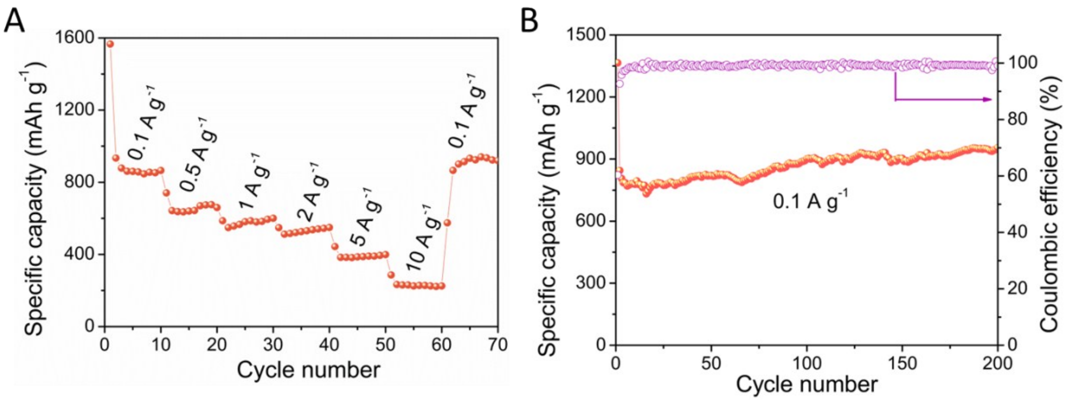

Fig. S22 Electrochemical performance of $Zn_{0.24}MnO$@C HHNDs as anode materials of LIBs: (A) rate capability at various current densities and (B) cycling performance with corresponding Coulombic efficiency at a current density of 0.1 A g^{-1}.

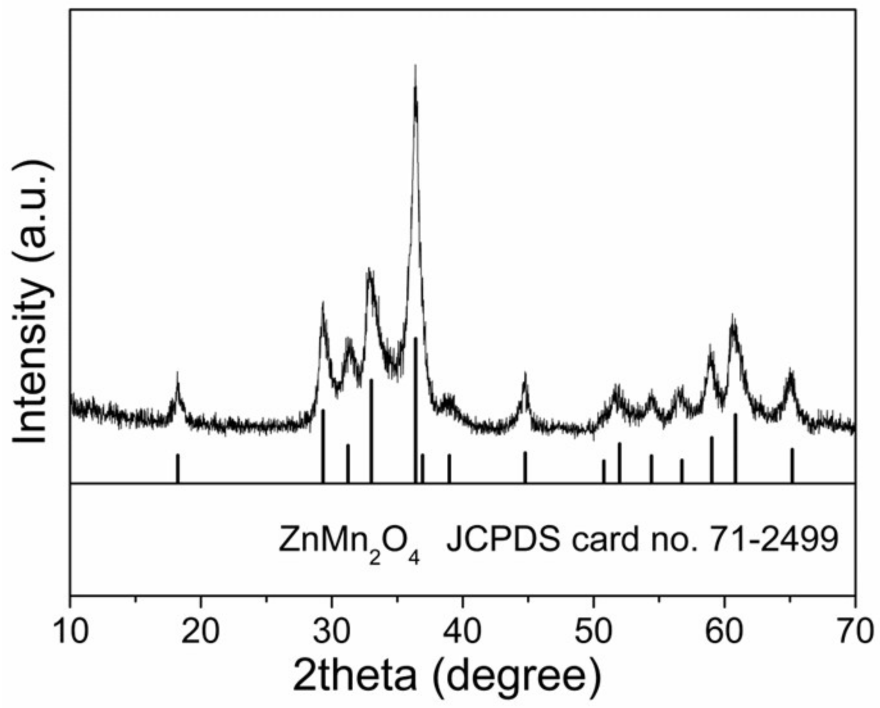

Fig. S23 XRD pattern of pure $Zn_{0.5}MnO$ material prepared by annealing Zn-Mn-BTC-0.5 precursor at 500 ℃ in air.

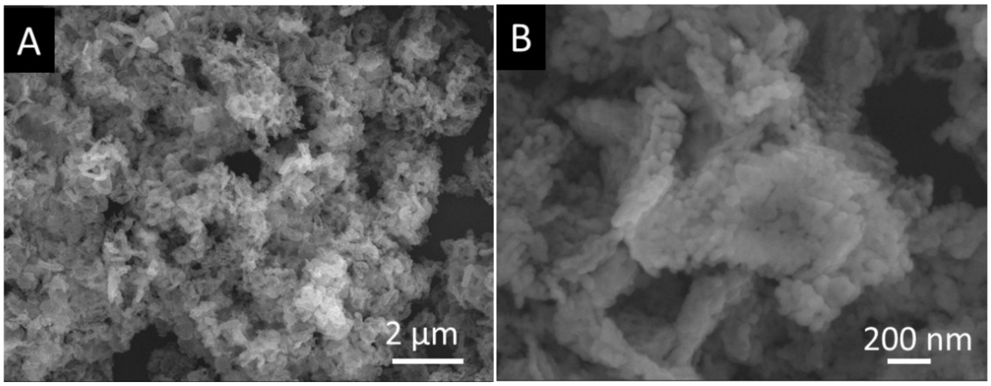

Fig. S24 FESEM images of pure $Zn_{0.5}MnO$ material prepared by annealing Zn-Mn-BTC-0.5 precursor at 500 ℃ in air.

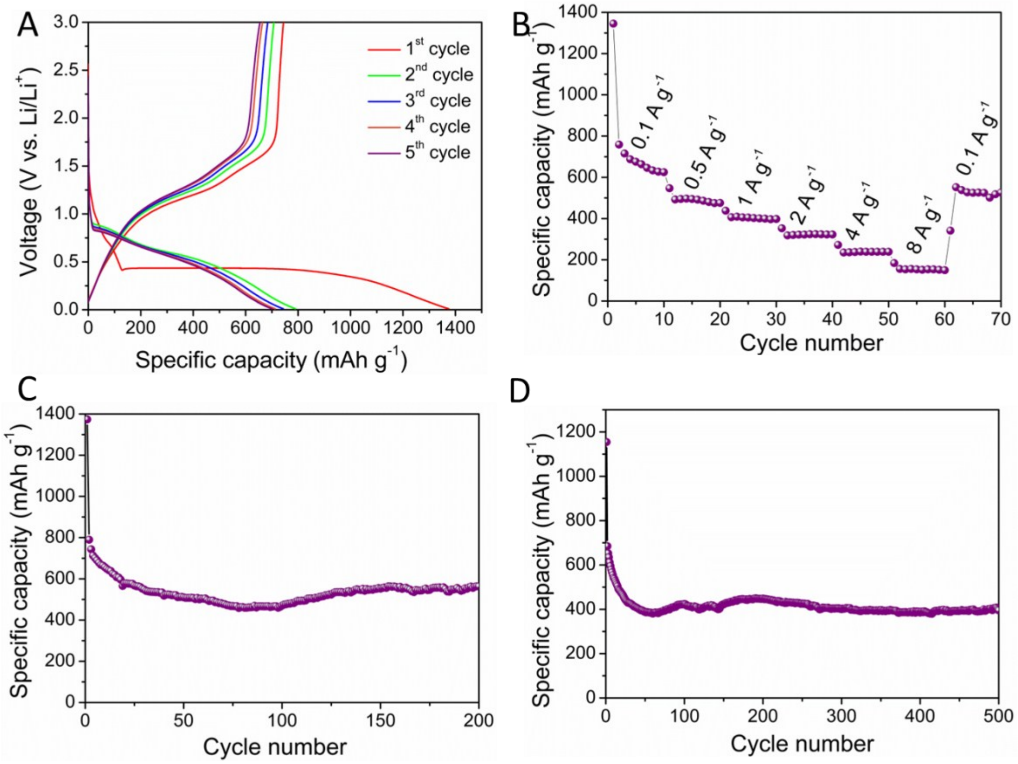

Fig. S25 Electrochemical performance of pure $Zn_{0.5}MnO$ materials as anode materials of LIBs: (A) galvanostatic discharge-charge voltage profiles at a current density of 0.1 A g^{-1} for the initial 5 cycles, (B) rate capability at current densities from 0.1 to 8 A g^{-1}, (C) cycling performance at a current density of 0.1 A g^{-1}, and (D) cycling performance at a current density of 0.5 A g^{-1}.

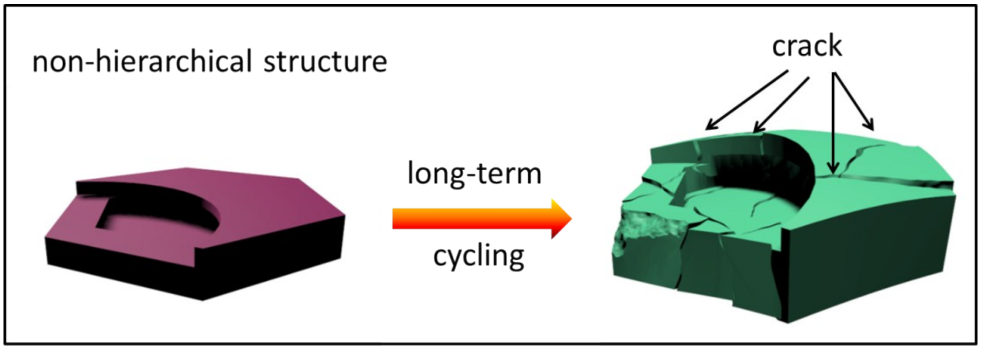

Fig. S26 Schematic illustration of the structure evolution of non-hierarchical counterpart after repeated discharge/charge cycles.

Table S1. Elemental analysis (EA) result of hierarchical $Zn_{0.5}MnO@C$ HHNDs.

Element	**N**	**C**	**H**
Weight percent (%)	1.49	26.93	1.01

Reference

1 X. Liu, C. Zhao, H. Zhang and Q. Shen, *Electrochim. Acta* 2015, **151**, 56.

2 M. Zhong, D. Yang, C. Xie, Z. Zhang, Z. Zhou and X.-H. Bu, *Small* 2016, **12**, 5564.

3 M. S. Song, S. Nahm, W. I. Cho and C. Lee, *Phys. Chem. Chem. Phys.* 2015, **17**, 23496.

4 N. Wang, X. Ma, H. Xu, L. Chen, J. Yue, F. Niu, J. Yang and Y. Qian, *Nano Energy* 2014, **6**, 193.

5 Y. Liu, J. Bai, X. Ma, J. Li and S. Xiong, *J. Mater. Chem. A* 2014, **2**, 14236.

6 Z. Zheng, Y. Cheng, X. Yan, R. Wang and P. Zhang, *J. Mater. Chem. A* 2014, **2**, 149.

7 J. G. Kim, S. H. Lee, Y. Kim and W. B. Kim, *ACS Appl. Mater. Interfaces* 2013, **5**, 11321.

8 G. Zhang, L. Yu, H. B. Wu, H. E. Hoster and X. W. Lou, *Adv. Mater.* 2012, **24**, 4609.